

Dependence of the ratio of total to visible mass on observable properties of SDSS MaNGA galaxies

KELLY A. DOUGLASS¹ AND REGINA DEMINA¹

¹*Department of Physics & Astronomy, University of Rochester, 500 Wilson Blvd., Rochester, NY 14611*

ABSTRACT

Using spectroscopic observations from the SDSS MaNGA DR15, we study the relationships between the ratio of total to visible mass and various parameters characterizing the evolution and environment of the galaxies in this survey. Measuring the rotation curve with the relative velocities of the H α emission line across a galaxy’s surface, we estimate each galaxy’s total mass. We develop a statistical model to describe the observed distribution in the ratio of total to visible mass, from which we extract a galaxy’s most probable value for this mass ratio. We present the relationships between the ratio of total to visible mass and several characteristics describing galactic evolution, such as luminosity, gas-phase metallicity, distance to the nearest neighbor, and position on the color-magnitude diagram. We find that faint galaxies with low metallicities, typically in the blue cloud, have the highest ratios of total to visible mass. This mass ratio is significantly reduced when we include the H I mass in the total visible mass, implying that feedback mechanisms are not as strong in low-mass galaxies as previously thought. Those galaxies that exhibit the second highest ratios of total to visible mass are the brightest with high metallicities, typically members of the red sequence or green valley. AGN activity is likely both the quenching mechanism and the feedback that drives the mass ratio higher in these massive galaxies. Finally, we introduce a parametrization that predicts a galaxy’s ratio of total to visible mass based only on its photometry and luminosity.

1. INTRODUCTION

Current cosmological models indicate that the majority of matter in the universe is composed of dark matter (Planck Collaboration et al. 2020): material that interacts primarily through gravity. Observational evidence for dark matter exists across most scales in the universe, from gravitational lensing of galaxy clusters (Bartelmann 2010, and references therein) to galaxy kinematics (e.g., Freeman 1970; Bosma 1978; Carignan & Freeman 1985; Salucci 2019). Dark matter simulations are able to reproduce the current distribution of galaxies (e.g., Springel et al. 2005), indicating that dark matter’s evolution throughout cosmic time dictates the formation and evolution of galaxies.

Understanding the quantity and distribution of dark matter in galaxies is crucial to our studies of galaxy formation and evolution. To this end, we need to measure how much dark matter exists in galaxies, and we need to understand how the ratio of dark to visible matter influences a galaxy’s star formation history. Previous studies

of the relationship between the ratio of either dark matter or total mass to visible mass or luminosity show that faint galaxies have the most dark matter relative to their stellar mass and that the brightest galaxies have more dark matter than those of intermediate luminosity (Percic et al. 1996; Strigari et al. 2008; Torres-Flores et al. 2011; Karukes & Salucci 2017; Ouellette et al. 2017; Wechsler & Tinker 2018; Behroozi et al. 2019; Di Paolo et al. 2019; Douglass et al. 2019; Aquino-Ortíz et al. 2020). In addition, Behroozi et al. (2019) found that massive quenched galaxies reside in more massive halos than star-forming galaxies of the same stellar mass.

In this paper, we utilize the SDSS MaNGA survey (Bundy et al. 2015) to investigate the possible relationships of a galaxy’s total, or dynamical, mass with its star formation history and local environment. We use the relative velocities of the H α emission line across a galaxy’s surface to measure the rotation curve of each galaxy, from which we estimate the galaxy’s total mass, M_{tot} . The sum of the stellar mass, M_* , and the H I mass estimates the total visible mass, M_{vis} , in each galaxy. We present the correlation of $M_{\text{tot}}/M_{\text{vis}}$ with various galaxy properties related to the galaxy’s star formation history and environment.

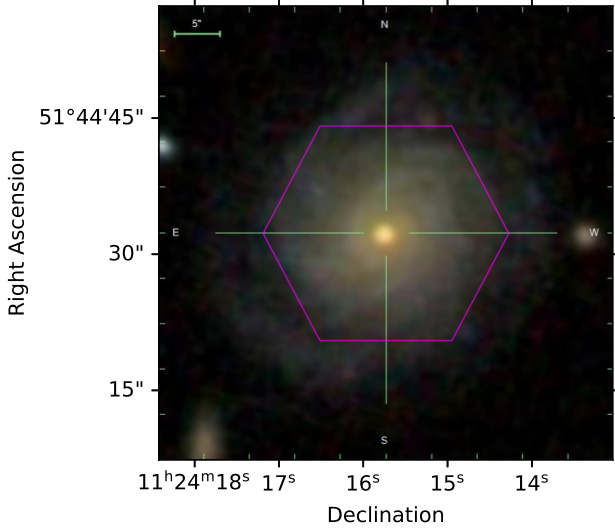


Figure 1. Example RGB composite image of a MaNGA galaxy (8997-9102) with the IFU (magenta hexagon) overlaid (made with the SDSS Marvin python package by Cherinka et al. 2019). As is typical with the MaNGA observations, the IFU does not cover the entire visible component of the galaxy.

Statistical and systematic uncertainties on the measured rotational velocity introduce a significant amount of variation in the resulting ratios of total to stellar mass between the galaxies in the sample. To adjust for this, we construct a statistical model that allows us to constrain the experimental uncertainties while extracting a more accurate estimate of the average $M_{\text{tot}}/M_{\text{vis}}$ within each galaxy subsample. In addition, as discussed in Douglass et al. (2019) and visible in Figure 1, the MaNGA data coverage is limited to the visible extent of the galaxy and to the size of the fiber-optic bundle (the integral field unit, or IFU). Therefore, our measurement of the rotational velocity, $V(r)$, is limited to the covered region. We extrapolate our parameterization of the fitted rotation curve to estimate $V(r)$ at the 90% elliptical Petrosian radius, R_{90} , so that we study the same region of each galaxy.

Due to dark matter’s lack of interaction via the electromagnetic force, there are limited statistics of the dark matter content of galaxies. Studies have been restricted to measurements of weak gravitational lensing from galaxy stacking, which require assumptions about the galaxy’s dark matter content *a priori*, and to studies measuring the kinematics of a galaxy, which require multiple observations across the spatially resolved surface of the galaxy. These kinematic studies are limited to only the closest objects and require a significant amount of observation time for each object. To help alleviate these

constraints, we introduce a parameterization of the ratio of total to stellar mass in a galaxy that requires galaxy photometry and redshift and can therefore be used on a much larger galaxy sample.

2. SDSS MANGA DR15 AND GALAXY SELECTION

We model the rotation curves of the velocity maps extracted from the $H\alpha$ emission line of galaxies in SDSS MaNGA DR15 (Aguado et al. 2019). MaNGA measures spectra across the face of each observed galaxy by placing a bundle of spectroscopic fibers (IFU) on each galaxy. Each IFU contains between 19 and 127 fibers, covering between 12" to 32" (corresponding to either $1.5R_e$ or $2.5R_e$ ¹) of the surface of each galaxy (Drory et al. 2015). Two dual-channel spectrographs receive the light from the IFUs, covering a wavelength range of 3600–10300Å with a resolution of $\lambda/\Delta\lambda \sim 2000$.

At its conclusion, MaNGA will observe 10,000 nearby galaxies in the northern sky. As described by Wake et al. (2017), targeted galaxies were selected to optimize the observed spatial resolution while maintaining a uniform distribution in luminosity. The final galaxy selection is split into three components: the primary sample, for which each galaxy is observed out to $1.5R_e$, the secondary sample, where the surface coverage is extended out to $2.5R_e$, and the color-enhanced sample, augmenting the primary sample with low-mass red galaxies and high-mass blue galaxies. The $H\alpha$ velocity map and r -band image processed by MaNGA’s data analysis pipeline (DAP) are used to extract the galaxy’s rotation curve. The stellar mass density map processed by Pipe3D (Sánchez et al. 2016, 2018) is used to extract the galaxy’s stellar mass contained within the same region. Absolute magnitudes are taken from the NASA-Sloan Atlas (NSA; Blanton et al. 2011).

We use the KIAS-VAGC (Blanton et al. 2005; Choi et al. 2010) for photometric data (colors, color gradients, and inverse concentration indices) of the MaNGA galaxies. We make use of the MPA-JHU value-added catalog² for global emission line fluxes. Gas-phase metallicities are calculated using these flux ratios and the N2O2 diagnostic described by Brown et al. (2016); this method has an systematic ~ 0.1 dex uncertainty in the calculated metallicity.

All of these value-added catalogs (NSA, KIAS-VAGC, MPA-JHU) are based on the SDSS Data Release 7 (DR7; Abazajian et al. 2009) galaxy sample, which we use for finding a MaNGA galaxy’s nearest neighbor. SDSS DR7

¹ R_e is the effective radius, or the 50% Petrosian radius.

² Available at <http://www.mpa-garching.mpg.de/SDSS/DR7>

employed a drift scanning technique to conduct a wide-field multiband imaging and spectroscopic survey that covered approximately one quarter of the northern sky. A dedicated 2.5-m telescope at the Apache Point Observatory in New Mexico was used to take the photometric data in the five-band SDSS system: u , g , r , i , and z (Fukugita et al. 1996; Gunn et al. 1998). Galaxies with a Petrosian r -band magnitude $m_r < 17.77$ were chosen for follow-up spectroscopic analysis using two double fiber-fed spectrometers and fiber plug plates with a minimum fiber separation of $55''$ (Lupton et al. 2001; Strauss et al. 2002). The wavelength coverage of the spectrometers used in this first stage of SDSS had an observed wavelength range of $3800\text{--}9200\text{\AA}$ with a resolution of $\lambda/\Delta\lambda \sim 1800$ (Blanton et al. 2003).

H I mass estimates are from the H I–MaNGA Data Release 2 (Stark et al. 2021) and the final Arecibo Legacy Fast ALFA (ALFALFA) data release (Haynes et al. 2018). H I–MaNGA is designed to conduct follow-up observations of all MaNGA galaxy targets on the Robert C. Byrd Green Bank Telescope (GBT) in Green Bank, West Virginia. The second data release of this program contains observations of 2135 MaNGA galaxies. To supplement the GBT observations, Stark et al. (2021) also include a cross match of the MaNGA DR15 sample with ALFALFA, a blind, 2-pass drift survey detecting extragalactic H I that was conducted at the Arecibo Observatory in Arecibo, Puerto Rico. ALFALFA adds H I detections for 1021 MaNGA DR15 galaxies. There are a total of 844 galaxies with H I detections in our final galaxy sample.

2.1. Color-magnitude classification

To study the relationship between the mass ratio and the evolutionary stage of a galaxy, we separate the galaxies into populations in the color-magnitude diagram. Fainter, bluer galaxies generally belong to the blue cloud, while brighter, redder galaxies belong to the red sequence. Galaxies are theorized to transition between these two populations through the green valley (Martin et al. 2007). Our classification of the galaxies into one of these three populations is a modification of the photometric classification scheme described in Douglass (2017), which is based on the morphological classifications of Park & Choi (2005) and Choi et al. (2010). Galaxies are classified based on their inverse concentration index, c_{inv} , and their position in the color ($u-r$) – color gradient ($\Delta(g-i)$) plane. We define a phase angle θ such that

$$\theta = \tan^{-1} \left(\frac{-\Delta(g-i) + 0.3}{(u-r) - 1} \right). \quad (1)$$

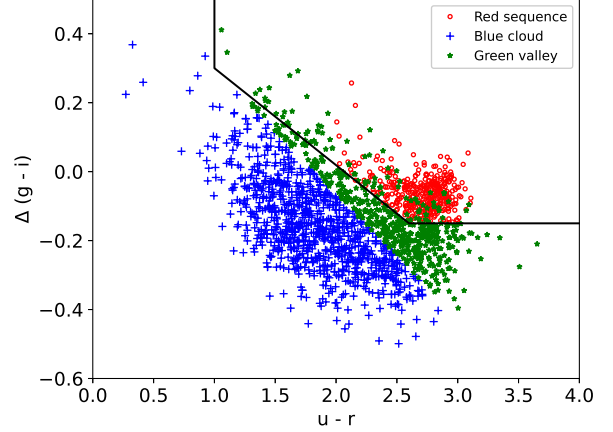


Figure 2. $\Delta(g-i)$ color gradient versus $u-r$ color for our sample of SDSS MaNGA galaxies, marked by their color-magnitude diagram classification: open red circles for the red sequence, green stars for the green valley, and blue crosses for the blue cloud. The black boundary is the separation between early- and late-type galaxies as defined by Park & Choi (2005).

We then classify the galaxy in either the blue cloud, green valley, or red sequence based on the following criteria:

Red sequence: Normal early-type galaxies (galaxies above the boundary defined by the points $(3.5, -0.15)$, $(2.6, -0.15)$, and $(1.0, 0.3)$ in the $u-r$ versus $\Delta(g-i)$ space with $u-r > 2$ and $c_{\text{inv}} \lesssim 3.8$).

Green valley: Blue early-type galaxies (galaxies above the boundary defined in the red sequence description with $u-r < 2$); Normal late-type galaxies that would otherwise be normal early-type galaxies except for their high c_{inv} ; Normal late-type galaxies (galaxies below the boundary defined in the red sequence description) with $\theta < 20^\circ$.

Blue cloud: Normal late-type galaxies (galaxies below the boundary defined in the red sequence description) with $\theta > 20^\circ$.

Figure 2 shows the results of this classification on our sample of SDSS MaNGA galaxies. Since we require our objects to be dominated by rotational motion as described below in Section 2.4, we would expect very few galaxies in our sample to be in the red sequence. However, we find a significant number of these objects in our final galaxy sample. Upon visual inspection, these galaxies appear to be a mixture of both red disk galaxies with little to no star formation and elliptical galaxies still supported by rotation.

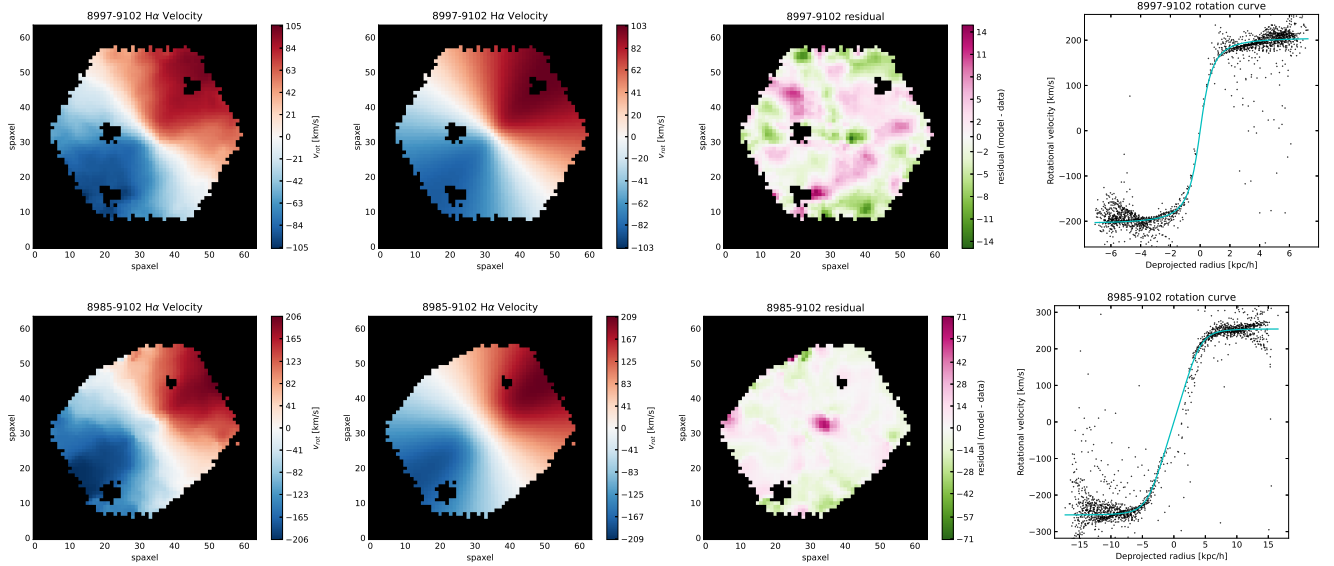


Figure 3. An example of the H α velocity map from the MaNGA DAP (first column), our best-fit model of the field (second column), the residual between our best-fit model and the data (third column), and the deprojected rotation curve (fourth column) for an unbarred spiral galaxy (Sc, top row) and barred spiral galaxy (SBbc, bottom row).

2.2. Modeling the velocity map

We use a galaxy’s H α velocity map to estimate its total dynamical mass. As provided by the SDSS MaNGA DAP, spaxels must have a data quality bit of 0 to be included in the analysis. Galaxies are also required to have velocity maps with a smooth gradient. See [Douglass et al. \(2019\)](#) for a more detailed explanation of this velocity gradient measurement.

Each velocity field is fit with the parameterization ([Barrera-Ballesteros et al. 2018](#)):

$$V(r) = \frac{V_{\max} r}{(R_{\text{turn}}^\alpha + r^\alpha)^{1/\alpha}} \quad (2)$$

where $V(r)$ is the tangential velocity at a given deprojected radius r , V_{\max} is the magnitude of the velocity at the rotation curve’s plateau, R_{turn} is the deprojected radius where the curve transitions from increasing to flat, and α is the degree of sharpness of the rotation curve. The free parameters in the fit are V_{\max} , R_{turn} , and α . We use this parameterization to determine the maximum rotational velocity for each galaxy, from which we can calculate the galaxy’s total mass. Future work will include a decomposition of the rotation curve into the various mass components (bulge, disk, halo) to study the structure of the dark matter halo in more detail. All distances are measured in units of Mpc/ h , where the reduced Hubble constant h is defined by $H_0 = 100h$ km/s/Mpc.

In addition to the three free parameters described above, we also fit for a galaxy’s systemic velocity, kinematic center, inclination angle, and rotation angle on

the sky. We iterate through different combinations of these parameters to find the model velocity map that best represents the data. See Figure 3 for example H α velocity maps and best-fit models.

We only model the rotation component of the velocity maps with this parameterization. It has been shown ([Valenzuela et al. 2007](#); [Randriamampandry et al. 2015](#); [Oman et al. 2019](#)) that rotational velocities can be over/underestimated when non-circular motions are not modeled in the central region of a galaxy, resulting from the presence of e.g., a bar. In this study, we are only concerned with estimating the maximum rotational velocity of the outer extent of the galaxy, where non-circular motion is negligible. Figure 3 shows both an unbarred (top row) and barred (bottom row) spiral galaxy. It is readily apparent that our parameterization of the velocity map successfully reproduces the rotational velocity component irrespective of morphological type.

We define the best model velocity map based on which model produces the smallest χ_ν^2 , where the fit statistic χ_ν^2 is normalized by the difference of the number of unmasked spaxels and the number of degrees of freedom of the fit (eight). We find this best-fit model map based on four different data masks:

Default: (spaxels with a data quality bit > 0 are masked) We find a best-fit model using this mask via two different criteria:

- The model with the smallest $\chi_\nu^2 = \sum((\text{data} - \text{model})/\text{uncertainty})^2$

- The model with the smallest residual, $\sum(\text{data} - \text{model})^2$

Continuous: (helps to mask foreground artifacts) We first bin all of the unmasked spaxels with a bin width of 10 km/s. Starting with the bin containing the most spaxels, we define the velocity bounds based on the first empty bin found in both directions from this central bin. All spaxels with velocities outside of this range are masked. We then find the model map that has the smallest χ^2_ν using this continuous mask.

High S/N: (removes spaxels with low S/N H α emission) We mask all spaxels with a S/N in the H α flux less than 5 and find the model which minimizes χ^2_ν .

No AGN: (helps to mask spaxels that likely contain emission from AGN, defined as bins with unusually high velocity dispersion) We first bin all unmasked spaxels in the H α velocity dispersion map with a bin width of 10 km/s. Starting with the bin containing 0 km/s, we define the velocity dispersion bounds based on the first empty bin found in both directions from this central bin. All spaxels with velocities outside of this range are masked. We then find the model map that has the smallest χ^2_ν using this non-AGN mask.

Of these five best-fit models, we select the map with the smallest χ^2_ν of those models with $\alpha < 100$.

To confirm that our best-fit models result in realistic galaxy kinematics, we plot the distribution of fitted maximum velocities as a function of the luminosity, M_r , and disk mass (the Tully-Fisher relation, TFR; Tully & Fisher 1977) in Figure 4. As expected, we find a strong positive correlation between the luminosity and maximum velocity. We also compare our baryonic TFR with the linear fits derived by Avila-Reese et al. (2008); Ferrero et al. (2017) and Aquino-Ortíz et al. (2018). As the left-hand plot in Figure 4 shows, our velocities agree with their results.

2.3. Modeling the stellar mass

To estimate the total stellar mass within the same radius for which we measure the total mass, we fit for the rotation curve due only to the stellar component of each galaxy. We use the kinematic center, inclination angle, and position angle on the sky from the best-fit model velocity map to define the ellipse which corresponds to a given orbital radius in the galaxy. Increasing the orbital radius in step sizes of 2 spaxels, we compute the sum of the stellar mass density per spaxel within these

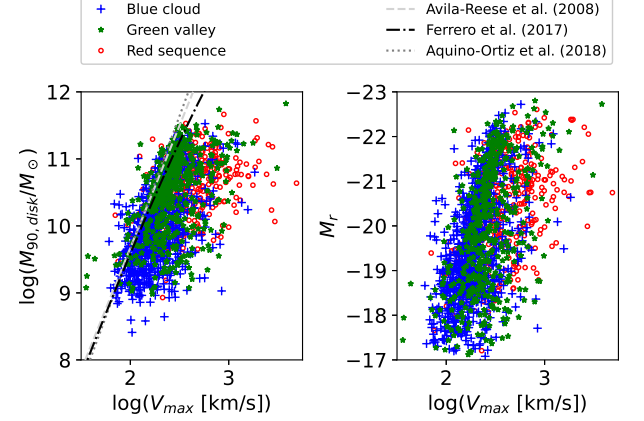


Figure 4. The Tully-Fisher relation (TFR) — the disk mass (left) and absolute magnitude in the SDSS r -band, M_r (right) as a function of the logarithm of the maximum velocity — for blue cloud (blue crosses), green valley (green stars), and red sequence (red circles) galaxies. For comparison, the linear relationships of the baryonic TFR derived in Avila-Reese et al. (2008); Ferrero et al. (2017) and Aquino-Ortíz et al. (2018) are shown on the left.

concentric ellipses of the stellar mass density map provided by the Pipe3D MaNGA analysis pipeline (Sánchez et al. 2016, 2018). An example of this stellar mass density map is shown on the left in Figure 5. With this, we have the stellar mass as a discretized function of radius, $M_*(r)$.

Assuming that the stellar mass is the primary component of the galaxy’s disk, we model the extracted stellar mass rotation curve as an exponential disk (a thin disk without perturbation; Freeman 1970), where

$$V_*(r)^2 = 4\pi G \Sigma_d R_d y^2 [I_0(y)K_0(y) - I_1(y)K_1(y)]. \quad (3)$$

Here, $V_*(r)$ is the rotational velocity due to the disk component of the galaxy, Σ_d is the central surface mass density of the disk, R_d is the scale radius of the disk, $y = r/2R_d$, and I_i and K_i are the modified Bessel functions (Sofue 2013). The free parameters in this fit are Σ_d and R_d . The total disk mass within some radius r is then

$$M_d(r) = 2\pi \Sigma_d \int_0^r r e^{-r/R_d} dr \quad (4)$$

$$= 2\pi \Sigma_d R_d \left[R_d - e^{-r/R_d} (r + R_d) \right]. \quad (5)$$

An example of the best fit to this stellar mass rotation curve is shown on the right in Figure 5. We compare our estimates of the disk mass within R_{90} to that derived by the Pipe3D analysis pipeline. As seen in Figure 6, the results of our fitting to the stellar mass density maps of Pipe3D are in good agreement with the Pipe3D estimates of the total stellar mass in the system.

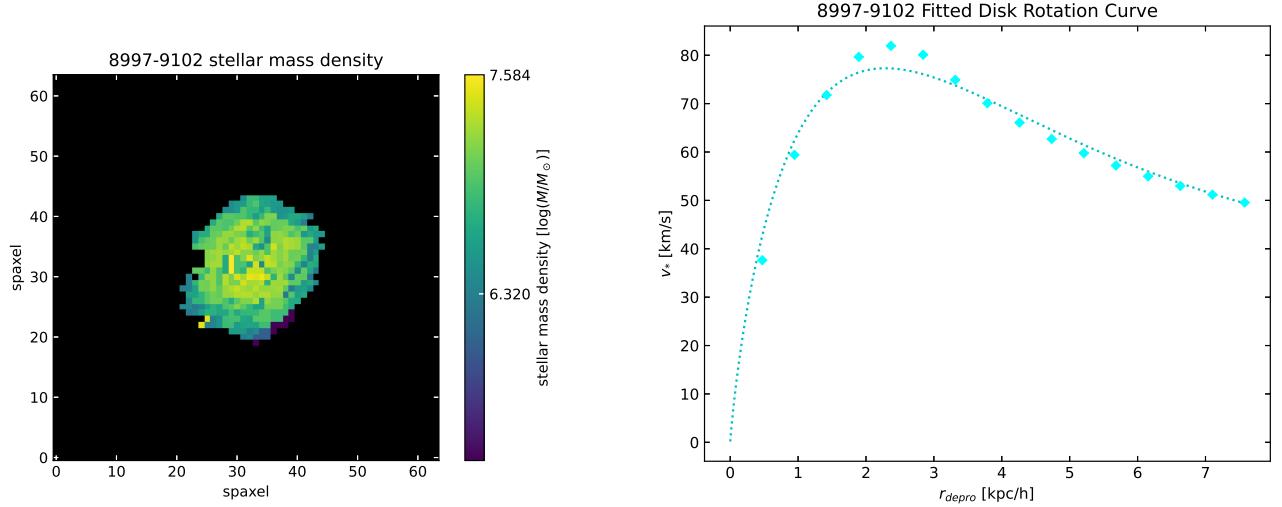


Figure 5. An example of the stellar mass density map from the Pipe3D analysis pipeline (left) and our best fit to the rotation curve extracted from this map (right).

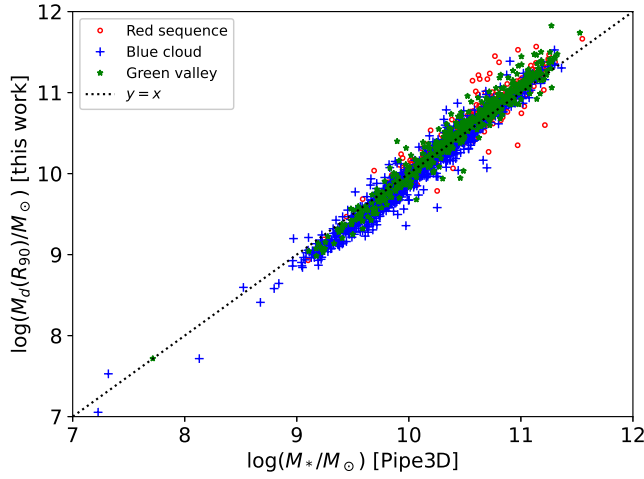


Figure 6. Comparison between our best-fit estimate of the disk mass within R_{90} , $M_d(R_{90})$, and the stellar mass, M_* , as derived by Pipe3D, for galaxies in the blue cloud (blue crosses), green valley (green stars), and red sequence (red circles). The black dotted line represents equality between the two quantities. There is good agreement between the two sets of measurements.

2.4. Galaxy selection criteria

After fitting both the H α velocity map and the stellar mass rotation curve, we restrict our sample to only include objects with successful fits for both of these models. We therefore reject any fit with

- $\alpha > 99$
- An inclination angle $> 86.4^\circ$
- Velocity maps with more than 95% of their data masked

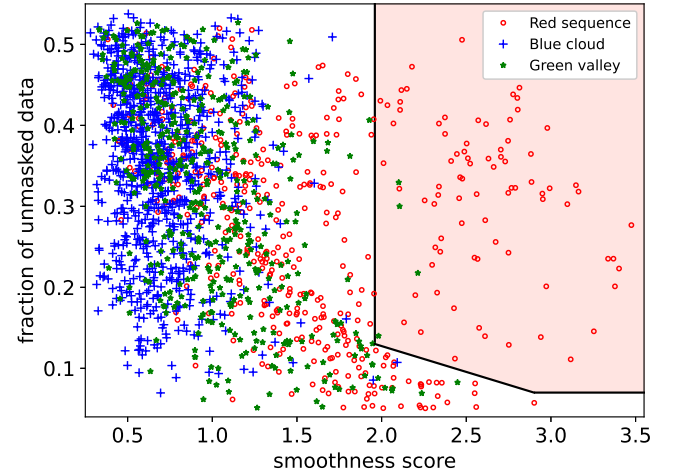


Figure 7. Relationship between the smoothness score and fraction of the velocity maps that are unmasked for those galaxies in our sample. Determined via visual inspection, objects above the black boundary (within the red shaded region) have velocity maps which do not exhibit rotational motion and are therefore excluded from our study.

The first two requirements remove fits with an unsuccessful minimization of χ^2_ν and therefore an untrustworthy and/or nonphysical model. To ensure that there are sufficient unmasked spaxels to fit, visual inspection revealed that no more than 95% of the total velocity map can be masked (this includes those data points outside the IFU footprint; for comparison, a completely unmasked IFU field corresponds to $\sim 55\%$ of the velocity map array unmasked).

Visual inspection of some of the stellar mass density maps produced by Pipe3D revealed that some

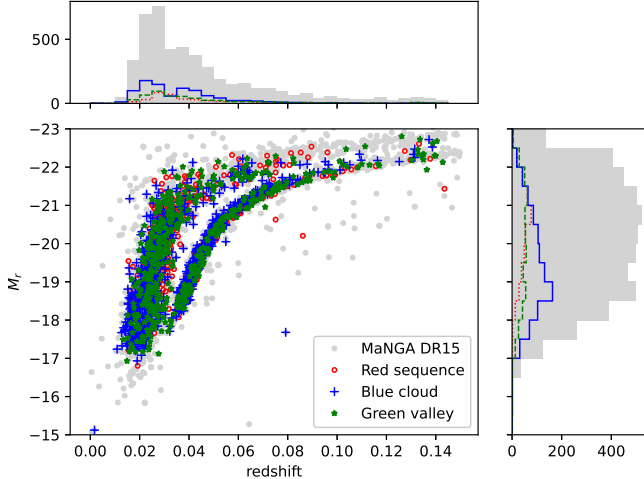


Figure 8. Distribution of our galaxy sample over luminosity and redshift. Galaxies classified as part of the blue cloud are shown as blue crosses, green valley galaxies are depicted as green stars, and red sequence objects are shown as open red circles. The corresponding distributions for each property are shown in the histograms, with the same colors as defined above. The entire SDSS MaNGA DR15 sample is shown in light gray.

maps have very sparse data and/or unrealistic stellar surface mass densities. Fitting to these maps results in an unexpectedly low estimate for $M_d(R_{90})$, and therefore an extremely high ratio of the total to disk mass, $M_{\text{tot}}/M_d(R_{90})$. We therefore also require that $M_{\text{tot}}/M_d(R_{90}) < 1050$.

We are focusing only on disc galaxies in this study (galaxies which are supported by rotation). Requiring a successful model velocity map by implementing the above criteria removes most elliptical galaxies, mergers, and interacting systems. We further remove all objects which have been determined to have some evidence of a disrupted velocity field. Using the visual morphological classifications from the MaNGA Visual Morphologies from SDSS and DESI images catalog³ and the morphological classifications from Domínguez Sánchez et al. (2018), we remove all objects with evidence of tidal debris (from the former) and a probability greater than 0.97 that it is a merger (from the latter). To ensure that there are no spurious elliptical galaxies that remain in our sample, we also remove all objects which lie above the boundary shown in Figure 7, defined by the points (1.96, 0.13) and (2.9, 0.07). Visual inspection of these

objects reveal that their velocity fields are dominated by random motion instead of rotation.

The proceeding analysis is conducted on a sample composed of disc galaxies. Since most elliptical galaxies are extremely bright, this introduces a selection bias towards fainter magnitudes. Our velocity parameterization of Eqn. 2 assumes a flat rotation curve, which therefore preferentially eliminates galaxies with low dark matter content (for which a rotation curve is dominated by the bulge’s mass). Of the 4815 galaxies with IFU spectra available in the Pipe3D analysis of the SDSS DR15 MaNGA survey, we successfully model the velocity map for 1988 galaxies. The distribution over luminosity and redshift for our final sample of galaxies (relative to the full SDSS MaNGA DR15) is shown in Figure 8.

3. ESTIMATING THE MASS COMPONENTS

3.1. Total mass

We assume that a galaxy’s rotational motion is dominated by Newtonian orbital mechanics: the orbital velocity of a particle some distance r from the center of the galaxy is a function of the total mass internal to that radius, $M(r)$, assuming axial symmetry. For spiral galaxies, the orbital motion is assumed to be circular. The gravitational force is the source of the centripetal acceleration for a particle in orbit, so

$$M(r) = \frac{V(r)^2 r}{G} \quad (6)$$

where $V(r)$ is the rotational velocity at a distance r from the center of the galaxy and $G = 6.67408 \times 10^{-11} \text{ m}^3 \text{ kg}^{-1} \text{ s}^{-2}$ is the Newtonian gravitational constant. Thus, by measuring $V(r)$ and r , we can estimate $M(r)$. Due to the limited extent of the MaNGA H α velocity maps, rotational velocities can only be measured out to the visible extent of the galaxy. As seen in Figure 1, the IFU coverage limits the maximum radius, R_{max} , to which the rotational curves are evaluated. Figure 9 (left) shows the distribution over R_{max} . We find that the maximum radius can be as high as 25 kpc/h, but the majority of the galaxies have data out to about 5 kpc/h.

To help alleviate this observational bias introduced by the size of the IFU, we use the parametrization of Eqn. 2 to extrapolate the rotation curve out to R_{90} , the distribution over which is shown Figure 9 (right). We then evaluate the galaxy’s total mass, M_{tot} , at this radius using Eqn. 6, as illustrated on the left in Figure 10 for a sample of randomly selected galaxies. In Figure 11, we present the distribution of the rotational velocity at R_{max} (left) and at R_{90} (right) normalized by the best-fit value obtained for V_{max} . It is apparent that the rotational curves are closer to the plateau in the latter case.

³ Available at https://www.sdss.org/dr16/data_access/value-added-catalogs/

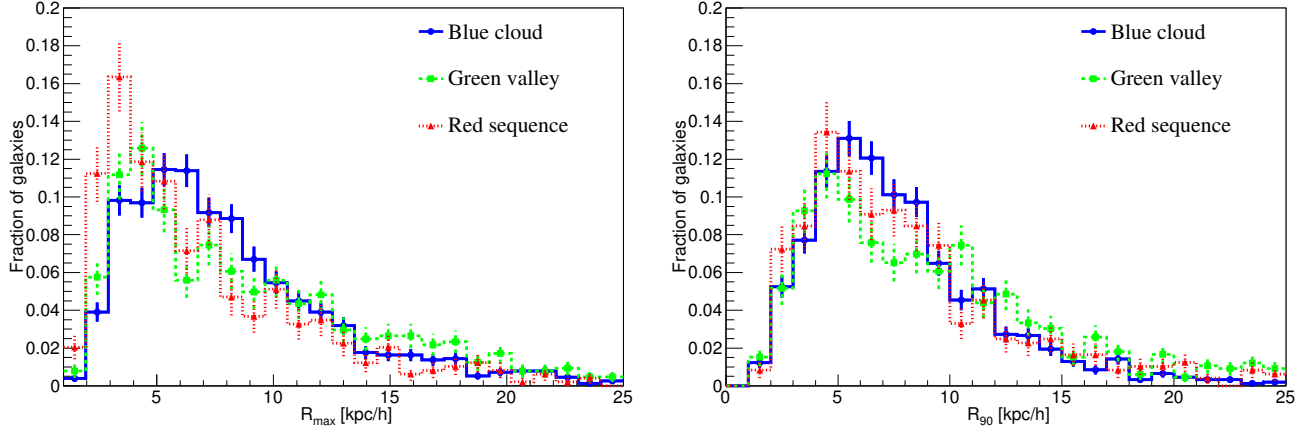


Figure 9. The distribution over the maximum radius to which the data extends (left) and 90% elliptical Petrosian light radius (right) to which the rotational curves are evaluated for blue cloud (blue solid line), green valley (green dashed line), and red sequence (red dotted line) galaxies.

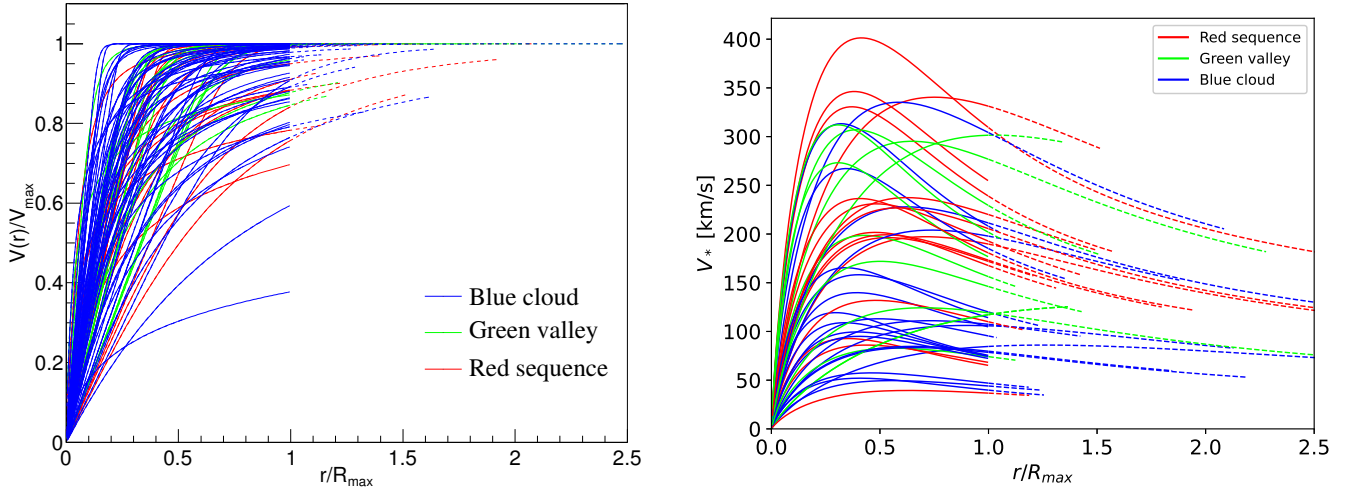


Figure 10. A sample of randomly selected rotation curves (left) and stellar mass rotation curves (right) for the blue cloud (blue), green valley (green), and red sequence (red) galaxies. The solid lines extend to $r = R_{\max}$, while the dashed lines show the curves extrapolated to $r = R_{90}$.

To ensure that the plateau is reached in further analysis we require that $V(R_{90})/V_{\max} > 0.90$. Not only does R_{90} typically extend further than R_{\max} , as shown in Figure 9, but evaluating the mass at R_{90} allows us to consistently probe the same region of each galaxy.

Previous studies (Cappellari et al. 2006; Weiner et al. 2006; Aquino-Ortíz et al. 2018) experimented with combining the rotation and random motion that support galaxies to better estimate the total dynamical mass of a galaxy. Defined as

$$S_K^2 = KV_{\max}^2 + \sigma^2 \quad (7)$$

where $K = 0.5$, V_{\max} is the maximum rotational velocity measured in the galaxy, and σ is the average velocity dispersion in the galaxy, this quantity is theorized to be

proportional to the galaxy’s total mass,

$$M_{\text{tot}} = \eta \frac{S_{0.5}^2 r}{G} \quad (8)$$

where $\eta \approx 1.8$ for $r = R_e$ (Aquino-Ortíz et al. 2018). We compare our estimates for the total mass, M_{tot} , with the dynamical mass estimated with Eqn. 8 evaluated at R_{90} . As seen in Figure 12, we find good agreement between our results and the masses estimated with $S_{0.5}$. Those galaxies with the largest difference between these two masses are those with the smallest masses, $\log(M_{\text{tot}}/M_{\odot}) \lesssim 10.5$. These objects have very little velocity dispersion, indicating that they are dominated by rotation. This disagreement is therefore likely due to a different value of η or K for these objects. Investigating

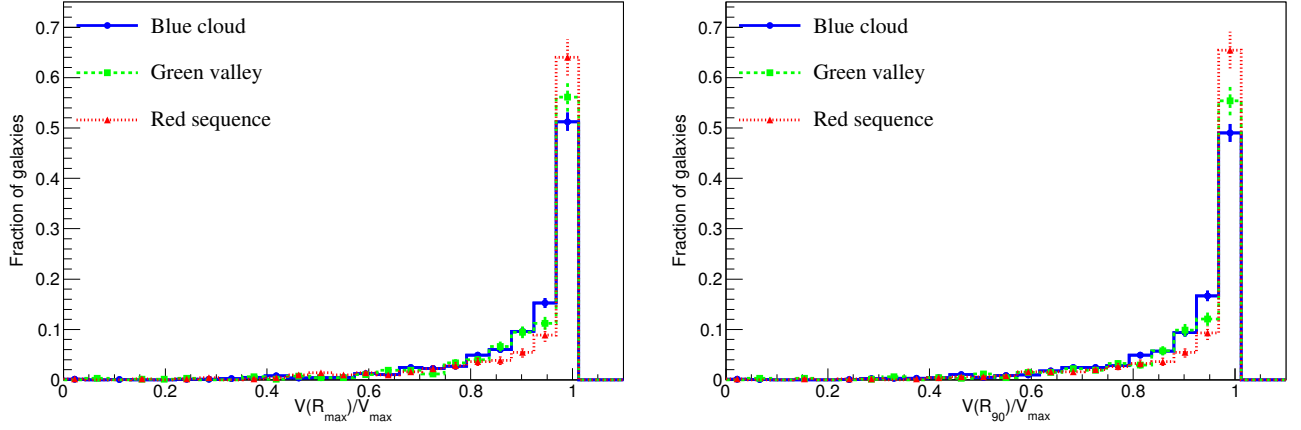


Figure 11. The distribution over the rotational velocity, $V_r(r)$, evaluated at R_{\max} (left) and at R_{90} (right) normalized by V_{\max} for the blue cloud (blue solid line), green valley (green dashed line), and red sequence (red dotted line) galaxies.

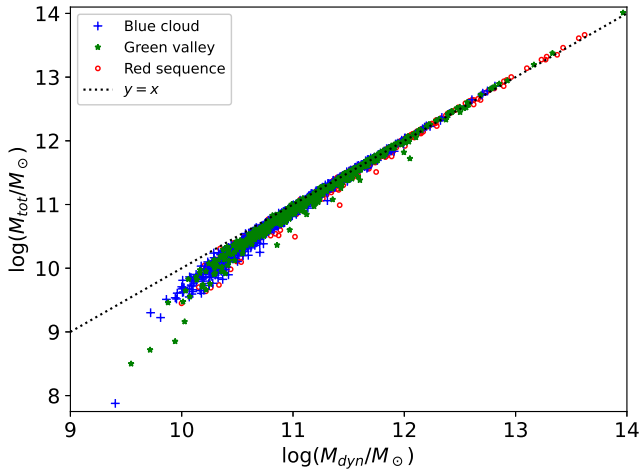


Figure 12. Relationship between the total mass, M_{tot} , and the dynamical mass, M_{dyn} , calculated using the kinematic parameter $S_{0.5}$, as defined in Aquino-Ortíz et al. (2018). The black dotted line represents the one-to-one relationship. We find good agreement with this other mass indicator, with our M_{tot} smaller than M_{dyn} at low mass.

the dynamical mass estimated with S_K with our sample is beyond the scope of this study.

3.2. Stellar mass, M_*

We estimate the total stellar mass, M_* , contained within R_{90} by extrapolating our fitted disk rotation curve out to R_{90} . We then evaluate the galaxy’s total stellar mass, M_* , at this radius using Eqn. 5, as shown on the right in Figure 10. The relationship between the stellar mass and total mass within R_{90} for our sample of galaxies is shown on the left in Figure 13. The points with error bars show the median total mass in each stellar mass bin for galaxies in each of the three evolutionary populations: blue cloud, green valley, and red sequence.

For galaxies with stellar masses above $10^{10} M_{\odot}$, we find that the total mass is approximately proportional to stellar mass, similar to the results of Ouellette et al. (2017); Aquino-Ortíz et al. (2020). We illustrate this by performing a linear fit to the data with a fixed slope of 1. The result of the fit is shown by a solid black line with the y -intercept of 0.70 ± 0.01 . Galaxies in each of the three evolutionary populations follow this relationship, though there is some deviation from it for lower stellar masses. Given the strong correlation between the total and stellar mass, we conclude that the ratio M_{tot}/M_* is an appropriate variable to study.

3.3. Neutral hydrogen, $M_{\text{H I}}$

We investigate the effect of the H I mass on the visible mass by combining it with the total stellar mass to estimate the total visible mass in a galaxy, M_{vis} . Due to the limited progress of the H I-MaNGA survey, only 844 galaxies in our sample currently have an H I detection. The relationship between the total mass and the visible mass that includes H I is presented on the right in Figure 13. The proportionality between these two quantities still holds, as is demonstrated by the linear fit with a fixed slope of 1 and a y -intercept of 0.46 ± 0.01 . As a result, we use the ratio $M(R_{90})/(M_*(R_{90}) + M_{\text{H I}}) = M_{\text{tot}}/M_{\text{vis}}$ in our study.

3.4. Statistical model for $M_{\text{tot}}/M_{\text{vis}}$

The accuracy of determining $M_{\text{tot}}/M_{\text{vis}}$ is limited by the statistical and systematic uncertainties on the rotational velocity at the 90% elliptical Petrosian radius, $V(R_{90})$. We develop a statistical model that accounts for the resolution on the rotational velocity and uncovers the true value of $M_{\text{tot}}/M_{\text{vis}}$, referred to as A_{true} . This model uses the data distribution in the observed $M_{\text{tot}}/M_{\text{vis}}$ to fit for the best value of the relative uncertainty on the rotational velocity σ_v together with A_{true} ,

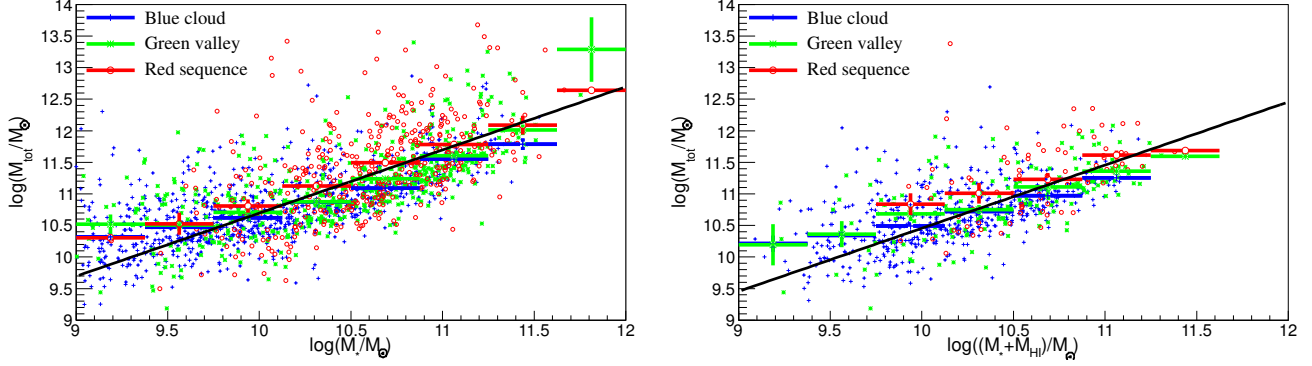


Figure 13. The relationship between the total mass and the stellar mass (left) and the visible ($M_* + M_{\text{HI}}$) mass (right) for each of the galaxies in our sample (points). The symbols correspond to the color-magnitude diagram classification: blue crosses are for the blue cloud, green asterisks for the green valley, and red open circles for the red sequence. Galaxies in each of these three populations are binned according to their stellar mass (left) or visible mass (right); the median total mass in each of these bins is shown in the points with error bars. The black line is a fit to the entire sample with a fixed slope of one and intercept of 0.70 ± 0.01 (left) and 0.46 ± 0.01 (right).

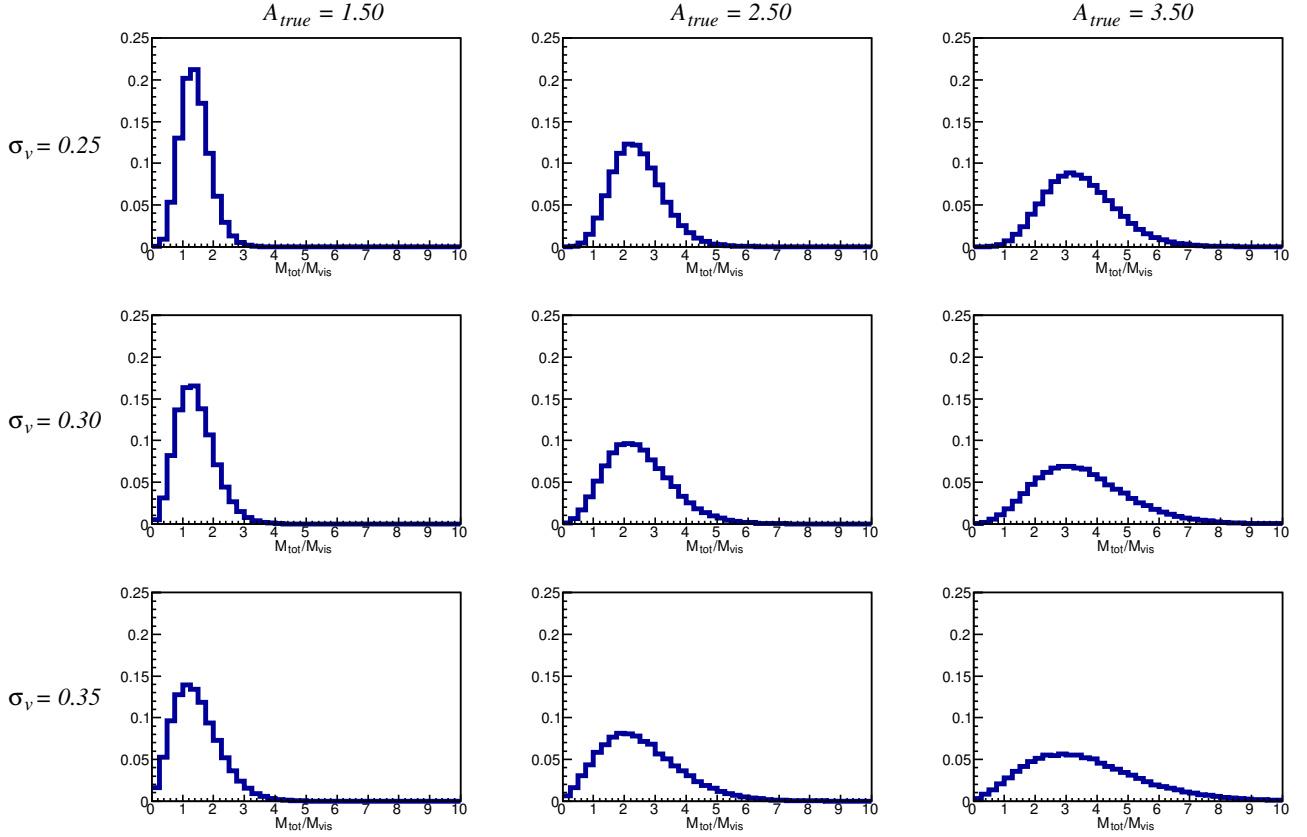


Figure 14. Templates in $M_{\text{tot}}/M_{\text{vis}}$ with different values of A_{true} (changing horizontally from 1.0 to 2.0) and σ_v (changing vertically from 0.25 to 0.35).

which should be understood as a mean true value for a sample of galaxies included in the fit.

We assume that the best-fit maximum velocity $V_{\max, \text{obs}}$ is normally distributed around its true value V_{true} with the standard deviation of $\sigma_v V_{\text{true}}$. We also assume that M_{tot} is equal to the product of the measured value of the visible mass, M_{vis} , and A_{true} . We construct template distributions in $M_{\text{tot}}/M_{\text{vis}}$ for several values of A_{true} and σ_v . To build a given template, we multiply each galaxy's M_{vis} by the template's value of A_{true} to estimate the galaxy's total mass. From the total mass, we calculate the true value of the velocity, V_{true} , using the relation given in Eqn. 6 with $r = R_{90}$. V_{true} is then smeared according to a normal distribution with standard deviation $\sigma = V_{\text{true}}\sigma_v$, where σ_v is the value of the relative uncertainty on the rotational velocity assumed in this template. This normal smearing is repeated 100 times to construct smoother templates. The smeared velocity, V_{obs} , is then converted back into an “observed” total mass, from which we then calculate the “observed” mass ratio $M_{\text{tot}}/M_{\text{vis}}$. The procedure is repeated for all galaxies in a given sample. Thus, each template histogram has 100 times more entries than the data histogram.

For illustration, we show an example 3×3 template matrix in Figure 14. Since M_{tot} depends on V_{\max}^2 , a symmetric distribution in V_{\max} results in an asymmetric distribution in the observed $M_{\text{tot}}/M_{\text{vis}}$ with a preference for larger values of $M_{\text{tot}}/M_{\text{vis}}$. As can be seen from these plots, larger values of A_{true} result in the peak of the distribution being shifted towards larger values of the observed $M_{\text{tot}}/M_{\text{vis}}$, while larger values of σ_v result in a broadening of the distributions. Thus, comparing the templates with the data distributions constrains both parameters.

We construct templates for seven different values of A_{true} and seven different values of σ_v , resulting in 49 templates. To identify which combination of A_{true} and σ_v best represents the data, we evaluate the agreement of each template with the data distribution using a χ^2_ν criterion. χ^2_ν is normalized by the number of the degrees of freedom, which is equal to the number of bins minus the three free parameters from the fit (normalization, A_{true} and σ_v). We keep σ_v as a free parameter of the fit to account for variation from sample to sample. The observed optimal values of σ_v vary from 0.17 to 0.3.

The advantage of this statistical model is that it constrains the uncertainties on the rotational velocity *in situ*. Since the uncertainty on the rotational velocity affects the width of the distribution in the mass ratio, the uncertainty on the velocity (either statistical or systematic) is constrained by the fit itself.

Previous observations of the stellar-halo mass relation (SHMR) show that $M_{\text{tot}}/M_{\text{vis}}$ varies among a galaxy population (Wechsler & Tinker 2018, and references therein), so the fitted value of A_{true} should be understood as an average value of $M_{\text{tot}}/M_{\text{vis}}$ in a given population. The developed statistical model provides a good description of the data. In particular, a normal distribution in V_{obs} rather than in $M_{\text{tot}}/M_{\text{vis}}$ explains the asymmetric shape of the distribution over $M_{\text{tot}}/M_{\text{vis}}$. Deviations from the model for large values of $M_{\text{tot}}/M_{\text{vis}}$ can be attributed either to non-gaussian tails in the experimental uncertainties or to large deviations from the average in $M_{\text{tot}}/M_{\text{vis}}$ in a particular population.

4. CORRELATION OF THE MASS RATIO WITH EVOLUTIONARY AND ENVIRONMENTAL PROPERTIES

4.1. Dependence of the mass ratio on the color-magnitude classification

Due to the observed differences in the relationships between M_* and M_{tot} for the blue cloud, green valley, and red sequence galaxies seen in Figure 13, we perform the template fitting to these three populations separately. The results of the template fit to M_{tot}/M_* and $M_{\text{tot}}/M_{\text{vis}}$ are shown in Figure 15. Each of these plots demonstrates that the statistical model provides a good description of the data distributions. The best fit results and medians of the corresponding distributions in the observed M_{tot}/M_* and $M_{\text{tot}}/M_{\text{vis}}$ are summarized in Table 1. Medians, which are extracted from the data distributions without the use of the statistical model, would be equal to the best-fit values of A_{true} should the data follow the model's prediction exactly. The observed medians follow the same trend as the values of A_{true} but are generally somewhat higher due to deviations in the data distributions from the model's predictions, predominantly at the high values of M_{tot}/M_* and $M_{\text{tot}}/M_{\text{vis}}$ (the “tails” of the distributions). These deviations are reduced once the H I mass is included. Both the median and A_{true} values suggest that galaxies in the blue cloud have the highest values of both M_{tot}/M_* and $M_{\text{tot}}/M_{\text{vis}}$.

Galaxies in the blue cloud, green valley, and red sequence have different properties. As shown in Salim (2014); Douglass (2017); Coenda et al. (2018); Jian et al. (2020), galaxies in the red sequence are the brightest, most massive, and have the lowest star formation rates. Blue cloud galaxies are the opposite: they are the faintest, the least massive, and have the highest star formation rates. Galaxies in the green valley tend to have

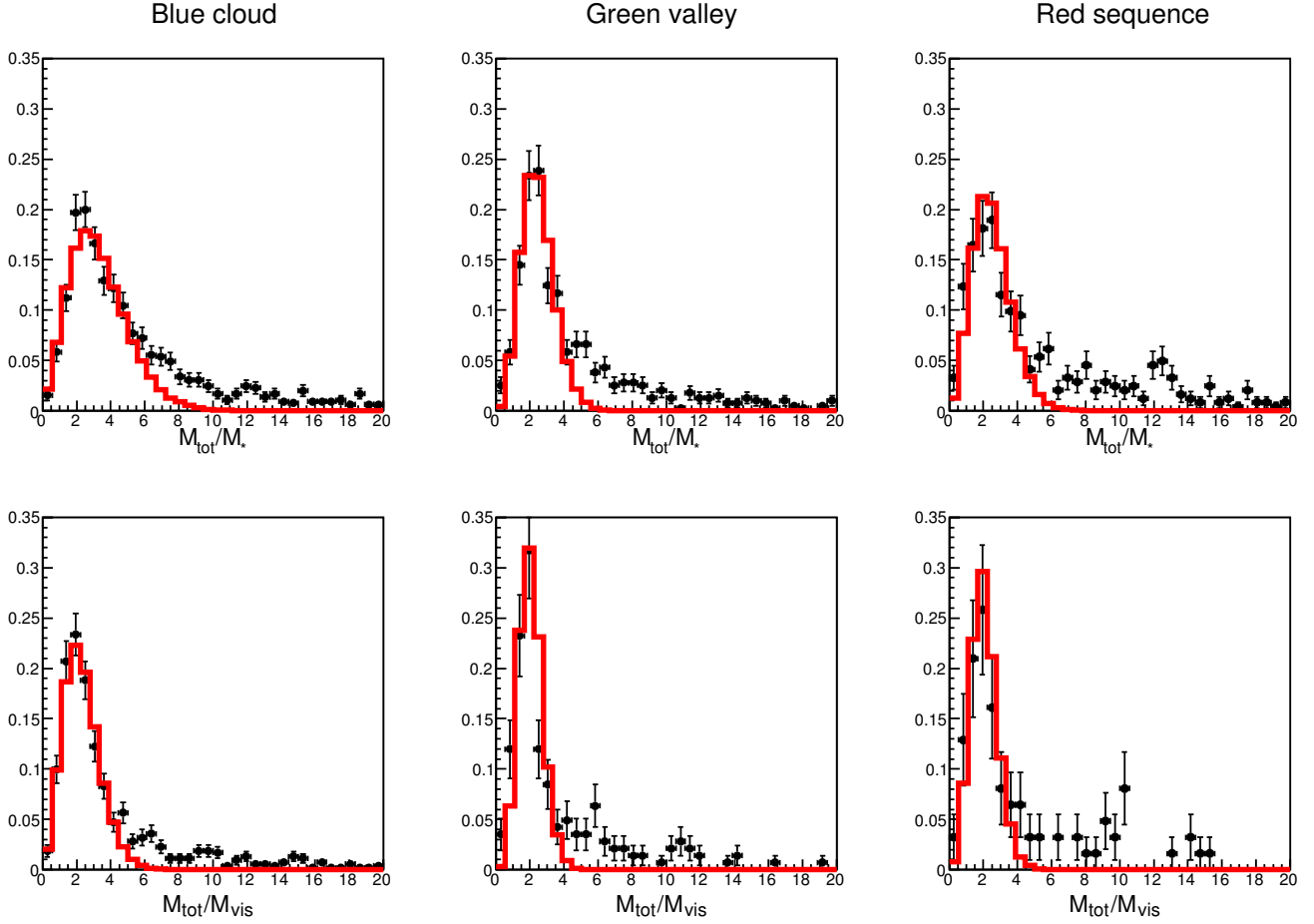


Figure 15. The distributions in M_{tot}/M_* (top row) and $M_{\text{tot}}/(M_* + M_{\text{HI}})$ (bottom row) for the sample of galaxies (points) compared to the model prediction based on the best fit template (histogram) for the three galaxy populations: blue cloud (left column), green valley (middle column), and red sequence (right column).

Table 1. Sample statistics and fitting results for galaxy classes

Class	Count	M_{tot}/M_*			$M_{\text{tot}}/(M_* + M_{\text{HI}})$	
		A_{true}	Median	Count with H I	A_{true}	Median
Blue cloud	931	3.10 ± 0.26	3.91 ± 0.12	531	2.20 ± 0.20	2.58 ± 0.14
Green valley	493	2.37 ± 0.22	3.02 ± 0.16	151	2.01 ± 0.37	2.19 ± 0.24
Red sequence	390	2.4 ± 0.27	3.52 ± 0.23	77	2.09 ± 0.54	2.47 ± 0.41

NOTE—The mass ratio values here correspond to the best-fitting template’s A_{true} . The median values correspond to the median of the distribution of M_{tot}/M_* and $M_{\text{tot}}/M_{\text{vis}}$ in the data.

luminosities and stellar masses comparable to those in the red sequence, but their star formation rates are intermediate.

Therefore, galaxies in the blue cloud are actively forming stars, while galaxies in the red sequence have undergone processes which have quenched their star formation. Green valley galaxies are either currently undergoing these quenching processes (moving from the blue cloud to the red sequence), or their star formation is restarting (transitioning from the red sequence to the blue cloud). Similar to [Torres-Flores et al. \(2011\)](#), we observe that the blue cloud galaxies have the highest values of M_{tot}/M_* and $M_{\text{tot}}/M_{\text{vis}}$. This trend is reduced once M_{HI} is included. These observations suggest a correlation between M_{tot}/M_* or $M_{\text{tot}}/M_{\text{vis}}$ and the current state of star formation. We test this hypothesis by investigating the relationships between both M_{tot}/M_* and $M_{\text{tot}}/M_{\text{vis}}$ and several galaxy properties related to the galaxy’s evolution history and its local environment.

4.2. Dependence of the mass ratio on luminosity and gas-phase metallicity

We study the dependence of M_{tot}/M_* and $M_{\text{tot}}/M_{\text{vis}}$ on a galaxy’s luminosity, M_r , and gas-phase metallicity, $12 + \log(\text{O}/\text{H})$, defined as the relative abundance of oxygen to hydrogen. Galaxies typically follow the mass-metallicity relation (e.g., [Tremonti et al. 2004](#)), where more massive galaxies have higher metallicities. While a galaxy’s metallicity should depend on its stellar mass, it should also increase with its total mass due to the corresponding deeper potential well. As shown in [Douglass \(2017\)](#), blue cloud galaxies have slightly lower metallicities than those in the red sequence, indicative of being in an earlier stage of their star formation histories. Similarly, red sequence galaxies are advanced in their star formation process and thus have higher metallicities.

While required to study these relationships, a fairly fine binning in M_r and $12 + \log(\text{O}/\text{H})$ does not permit a fit to the statistical model due to insufficient statistics in each bin. We instead extract the medians of the distribution in each bin. The statistical model is then applied to the coarsely binned data based on both M_r and $12 + \log(\text{O}/\text{H})$. On the left in Figure 16, we show the dependence of the median M_{tot}/M_* and $M_{\text{tot}}/M_{\text{vis}}$ values on the luminosity. We observe that the faintest galaxies (those with $M_r > -20$) have the largest value of mass ratio. This behavior agrees with prior observations by [Persic et al. \(1996\)](#); [Strigari et al. \(2008\)](#); [Torres-Flores et al. \(2011\)](#); [Karukes & Salucci \(2017\)](#); [Behroozi et al. \(2019\)](#); [Di Paolo et al. \(2019\)](#); [Douglass et al. \(2019\)](#) and the simulation results of [Moster et al. \(2010\)](#), who predict that faint galaxies are more enriched

in dark matter. Similar to these previous results, we also observe a rise in each of the mass ratios for the brightest galaxies, typically members of the red sequence type.

The relationship between each of the mass ratios and the gas-phase metallicity of the galaxies is shown on the right in Figure 16. Similar to the correlation between both M_{tot}/M_* and $M_{\text{tot}}/M_{\text{vis}}$ and M_r , we observe a rise in both M_{tot}/M_* and $M_{\text{tot}}/M_{\text{vis}}$ for galaxies with both high and low metallicities.

The addition of H I to the visible mass has a significant effect on faint galaxies and those with the lowest metallicities, while a smaller effect is observed for brighter, higher metallicity galaxies. This is similar to the observations made by [Torres-Flores et al. \(2011\)](#), who found that including M_{HI} in the total visible mass estimate reduced the deviation from the baryonic Tully-Fisher relation by the low-mass galaxies.

We further examine the dependence of both M_{tot}/M_* and $M_{\text{tot}}/M_{\text{vis}}$ on the luminosity and gas-phase metallicity by plotting each of the mass ratios in the 2D plane of $(M_r, 12 + \log(\text{O}/\text{H}))$, shown in Figure 17. We find that the highest values of $M_{\text{tot}}/M_{\text{vis}}$ are observed in faint galaxies with low metallicities and bright galaxies with high metallicities. To isolate these trends, we divide the galaxies into three categories as marked in the right panel of Figure 17, and perform a fit to the statistical model described in Section 3.4 to find the average value of both M_{tot}/M_* and $M_{\text{tot}}/M_{\text{vis}}$ in each of these three categories. The results of this fitting are presented in Figure 18 and summarized in Table 2.

It is apparent that higher values of both M_{tot}/M_* and $M_{\text{tot}}/M_{\text{vis}}$ are observed for faint galaxies with low metallicities (category 1), which is mostly populated by galaxies in the blue cloud. There is also an increase in both M_{tot}/M_* and $M_{\text{tot}}/M_{\text{vis}}$ for the brightest galaxies with the highest metallicities (category 3), populated predominantly by galaxies in the red sequence and green valley. Galaxies populating the central region of Figure 17 (category 2) have the lowest values of both M_{tot}/M_* and $M_{\text{tot}}/M_{\text{vis}}$. When comparing the top and bottom rows of Figure 18, we see that the addition of H I significantly reduces the tails in the distribution over the mass ratio, especially for those galaxies in category 1. This observed dependence on M_r and $12 + \log(\text{O}/\text{H})$ suggests a correlation of $M_{\text{tot}}/M_{\text{vis}}$ with a galaxy’s star formation history.

4.3. Estimating M_{tot}/M_* based on redshift and photometry

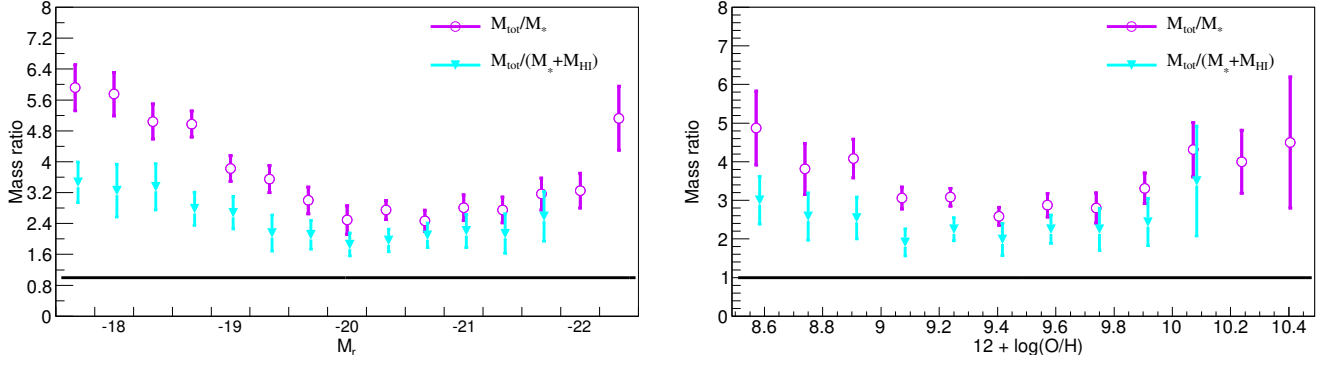


Figure 16. The dependence of median values of M_{tot}/M_* (open magenta circles) and $M_{\text{tot}}/(M_* + M_{\text{HI}})$ (filled cyan triangles) on the absolute magnitude, M_r (left), and gas-phase metallicity, $12 + \log(\text{O}/\text{H})$ (right). The solid black line represents a ratio of 1.

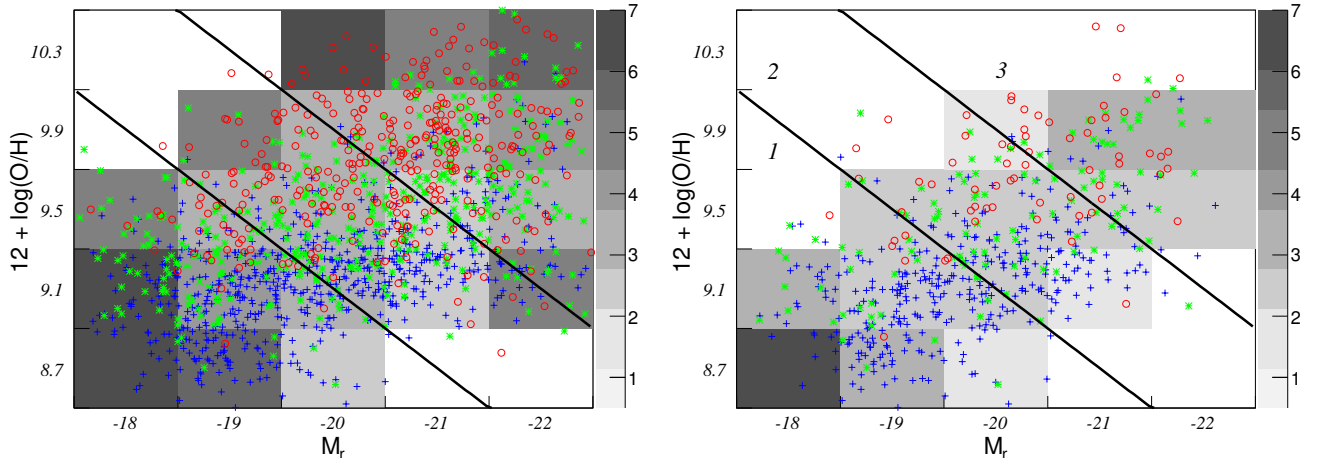


Figure 17. The grey scale shows the median values of M_{tot}/M_* (left) and $M_{\text{tot}}/(M_* + M_{\text{HI}})$ (right) in the bins of M_r and $12 + \log(\text{O}/\text{H})$. Overlaid are the galaxies in the blue cloud (blue crosses), green valley (green asterisks), and red sequence (red open circles). The solid diagonal lines ($12 + \log(\text{O}/\text{H}) = 0.4M_r + 17.1$ and $12 + \log(\text{O}/\text{H}) = 0.4M_r + 17.9$) indicate the boundaries for the three categories, labeled by the numbers in the right panel.

Table 2. Sample statistics and fitting results for galaxy categories

Category	Count	M_{tot}/M_*		Count with H I	$M_{\text{tot}}/(M_* + M_{\text{HI}})$	
		A_{true}	Median		A_{true}	Median
1	495	3.36 ± 0.46	4.25 ± 0.17	255	2.35 ± 0.31	2.64 ± 0.20
2	517	2.20 ± 0.21	2.67 ± 0.14	207	2.05 ± 0.27	2.07 ± 0.20
3	427	2.50 ± 0.26	3.15 ± 0.19	81	2.15 ± 0.46	2.32 ± 0.33

NOTE—Categories are as defined in Figure 17. All galaxies included in these fits are required to have gas-phase metallicity estimates. The mass ratio values here correspond to the best-fitting template's A_{true} . The median values correspond to the median of the distribution of M_{tot}/M_* and $M_{\text{tot}}/M_{\text{vis}}$ in the data.

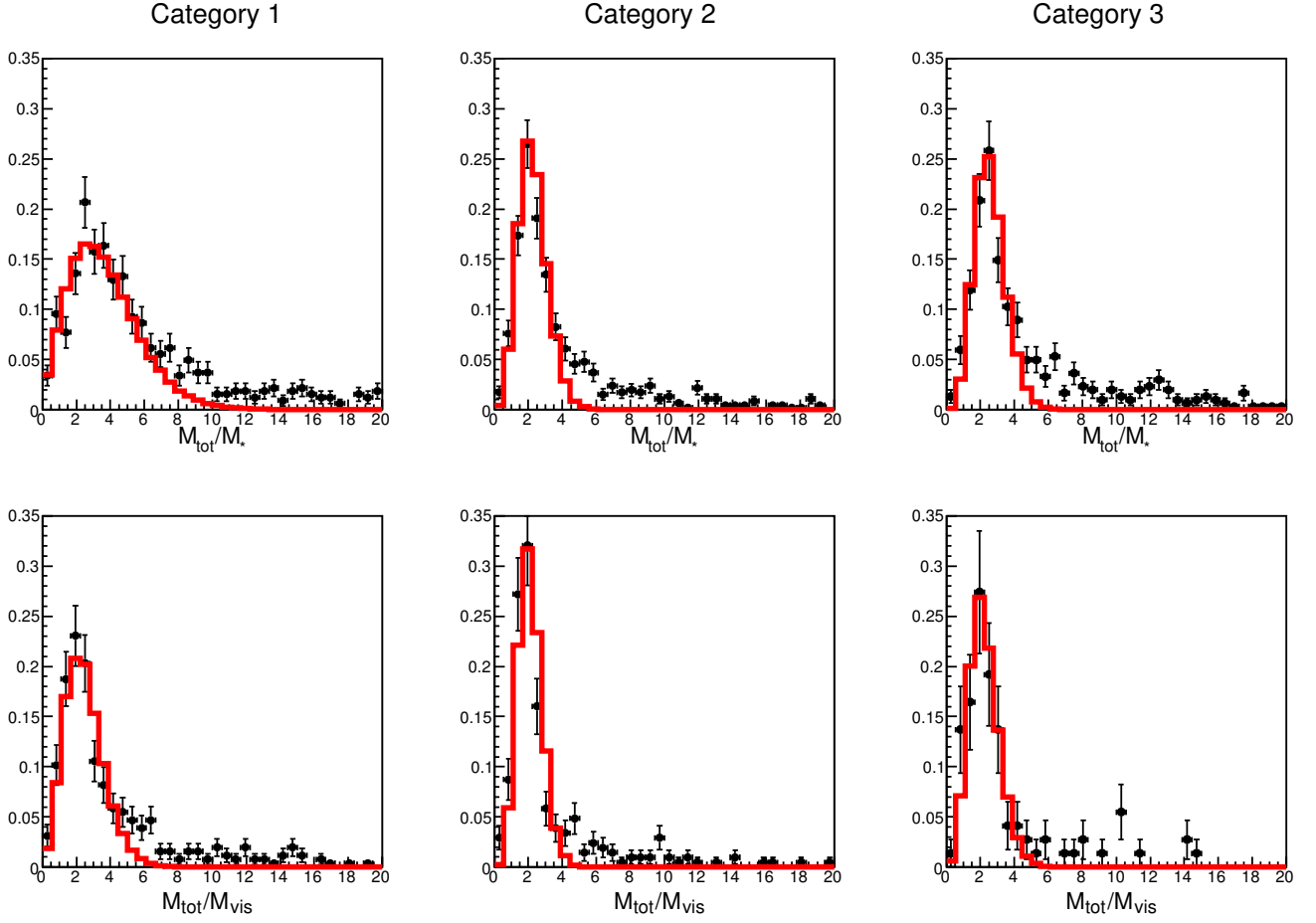


Figure 18. The distributions in M_{tot}/M_* (top row) and $M_{\text{tot}}/(M_* + M_{\text{HI}})$ (bottom row) for the sample of galaxies (points) compared to the model prediction based on the best fit template (histogram) for the three galaxy categories defined in Figure 17: 1 (left column), 2 (middle column), and 3 (right column).

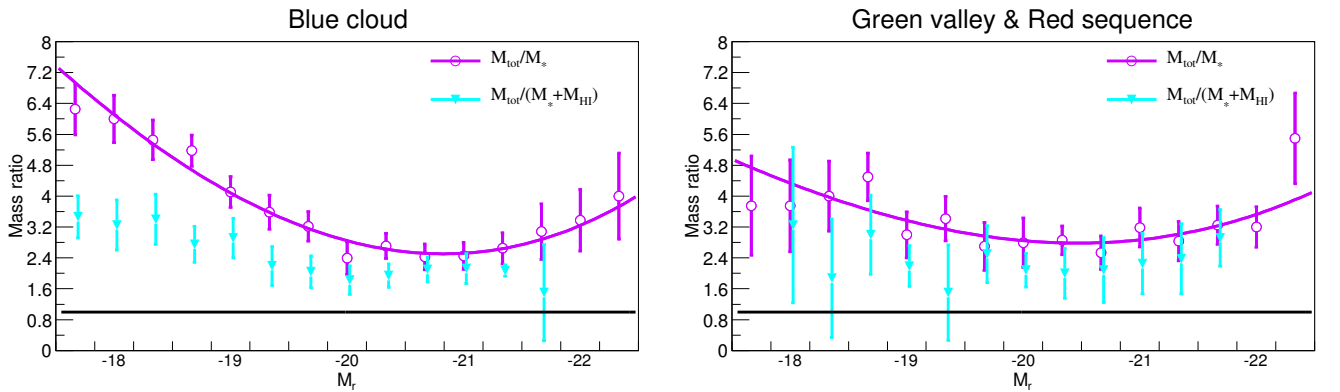


Figure 19. The dependence of median values of M_{tot}/M_* (open magenta circles) and $M_{\text{tot}}/(M_* + M_{\text{HI}})$ (filled cyan triangles) on M_r for galaxies in the blue cloud (left panel) and in the green valley and red sequence (right panel). The solid magenta lines show the best fits of M_{tot}/M_* to a third power polynomial.

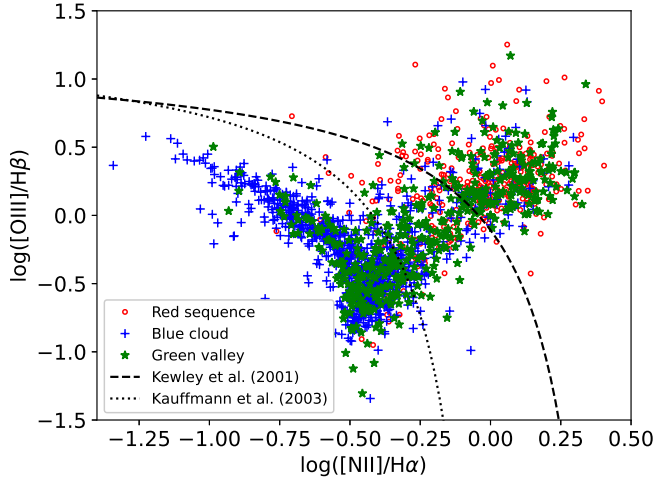


Figure 20. A BPT diagram for our sample of SDSS MaNGA galaxies, marked by their color-magnitude diagram classification: open red circles for the red sequence, green stars for the green valley, and blue crosses for the blue cloud. Objects below the dotted line defined by Kauffmann et al. (2003) are considered to have their main source of ionization from star formation, while objects above the dashed line defined by Kewley et al. (2001) are expected to have their main source of ionization from AGN activity. Galaxies in between the two lines are composite galaxies, where their ionization comes from both star formation and AGN activity.

There is a class of problems, e.g. Large Scale Structure (LSS) studies, where it is important to evaluate the ratio of halo to stellar mass based on some easily accessible observables. Due to the systematics and relatively high S/N spectra required for its calculation, the gas-phase metallicity is not easily obtainable. However, a galaxy’s luminosity and its color-magnitude classification can be easily evaluated based on photometry and a redshift. Thus, we derive a parametrization of M_{tot}/M_* based on these two observables. Because of the limited statistics in our current sample, we combine the green valley and red sequence galaxies for this parameterization. Fits to the third power polynomials for these two populations of galaxies (blue cloud and red sequence / green valley) are shown in Figure 19. The results of the best fits are summarized in Table 3.

This version of the stellar-halo mass relation (SHMR) exhibits its key characteristics: the fraction of dark matter decreases with increasing stellar mass for all but the brightest galaxies (Wechsler & Tinker 2018; Douglass et al. 2019, and others). As expected, galaxies in the blue cloud show a strong rise in M_{tot}/M_* at the faint end, while galaxies in the green valley and red sequence

exhibit an increase in M_{tot}/M_* for both the brightest and faintest galaxies. Contrary to Behroozi et al. (2019), we find that the brightest quenched/quenching galaxies (galaxies in the green valley and red sequence) exhibit similar M_{tot}/M_* to their star-forming counterparts. We also find that faint galaxies in the blue cloud have significantly more dark matter compared to galaxies of similar luminosity in the green valley and red sequence, consistent with the results of Aquino-Ortíz et al. (2020). The addition of M_{HI} has the most significant impact on these galaxies.

Various feedback processes that reduce the star formation efficiency are often cited as the source for the divergence from a constant SHMR: supernovae feedback in fainter galaxies, and AGN feedback in the brightest galaxies (Wechsler & Tinker 2018; Di Paolo et al. 2019). With galaxies in the blue cloud having higher star formation rates, we would expect these to behave more similar to the faint galaxies, and we can hypothesize that their deviation from a constant SHMR is largely due to supernovae feedback. On the other hand, galaxies in the green valley and red sequence have much lower star formation rates; their feedback is likely due to AGN, which is also potentially responsible for their quenched star formation.

To help probe the source of feedback in these galaxies, we look at where the galaxies fall in the Baldwin-Phillips-Terlevich (BPT; Baldwin et al. 1981) diagram. The relative amount of $[\text{OIII}] \lambda 5007 / \text{H}\beta$ to $[\text{NII}] \lambda 6584 / \text{H}\alpha$ determines whether a galaxy’s ionization source is primarily from star formation, AGN activity, or a combination of the two. We define the boundary between star-forming and composite galaxies as given in Kauffmann et al. (2003), and the boundary between composite and AGN galaxies is as defined by Kewley et al. (2001). The BPT diagram for our sample of galaxies is shown in Figure 20, where we see that most of the galaxies classified as being in the blue cloud are star-forming, while the red sequence objects are predominantly composite galaxies and AGN. Galaxies in the green valley span all three populations. This supports the hypothesis that the fainter, more metal-poor galaxies in the blue cloud (located on the upper left of the BPT diagram) deviate from a constant SHMR because of supernova feedback, while the feedback in the most massive, metal-rich galaxies in the red sequence and green valley (the upper right of the BPT diagram) is due to AGN activity.

4.4. Dependence of the mass ratio on the distance to the nearest neighbor

Table 3. Parameterization of M_{tot}/M_*

Class	p_0	p_1	p_2	p_3
Blue cloud	33.8 ± 1.1	6.10 ± 0.07	-0.80 ± 0.004	0.021 ± 0.0001
Green valley & Red sequence	-15.2 ± 1.5	8.66 ± 0.09	-0.72 ± 0.004	0.017 ± 0.0002

NOTE—Values of the best fit parameters to $M_{\text{tot}}/M_* = p_0 + p_1x + p_2x^2 + p_3x^3$, where $x = M_r$.

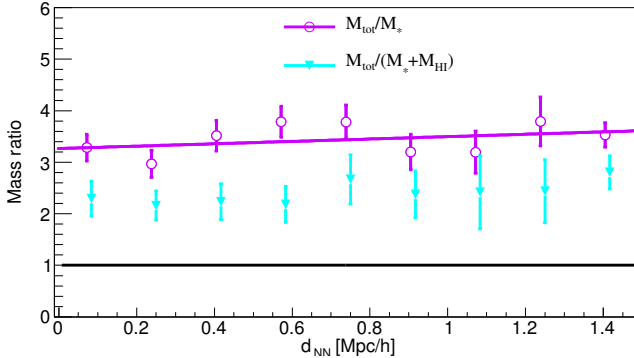


Figure 21. The relationship between the median values of M_{tot}/M_* (open magenta circles) and $M_{\text{tot}}/(M_* + M_{\text{HI}})$ (filled cyan triangles) and the distance to the nearest neighbor. The linear fit to M_{tot}/M_* is shown in the solid magenta line, with a slope of 0.23 ± 0.22 and a y -intercept of 3.27 ± 0.2 .

We investigate the effect of the local environment on both M_{tot}/M_* and $M_{\text{tot}}/M_{\text{vis}}$ by looking at the relationship between a galaxy’s mass ratio and the distance to its nearest neighbor, D_{NN} . We use the main galaxy sample of SDSS DR7 to find the potential neighbors. When calculating the distance to the nearest neighbor, we assume a flat geometry and use the linear approximation of Hubble’s law to define the radial distance from the Earth. The relationship between both M_{tot}/M_* and $M_{\text{tot}}/M_{\text{vis}}$ and D_{NN} is shown in Figure 21, where we observe an increase in the mass ratio with the distance from the nearest neighbor. This agrees with the simulation predictions of [Martizzi et al. \(2020\)](#), where galaxies in less dense environments are expected to have less stellar mass for a given dark matter halo mass. We surmise that this is because isolated galaxies tend to evolve slower than galaxies in denser regions, as isolated galaxies have lower probabilities of star formation episodes resulting from galaxy-galaxy interactions.

Figure 21 also shows that the relationship between the mass ratio and galaxy separation does not change with the inclusion of M_{HI} . This further supports that the decreasing $M_{\text{tot}}/M_{\text{vis}}$ with decreasing distance is a result of an increase in stellar mass, a sign that these galax-

ies have experienced more star formation as a result of galaxy-galaxy interactions.

5. CONCLUSIONS

We investigate the possible correlation between a galaxy’s ratio of total to stellar mass, M_{tot}/M_* , and visible mass, $M_{\text{tot}}/M_{\text{vis}}$, and its evolutionary population, luminosity, gas-phase metallicity, and local environment. We extract a galaxy’s rotation curve using the $\text{H}\alpha$ velocity maps from the SDSS MaNGA DR15, from which we estimate the galaxy’s total mass. We construct a statistical model that well describes the distribution over both M_{tot}/M_* and $M_{\text{tot}}/M_{\text{vis}}$ in the observed data while simultaneously evaluating the uncertainty in the measurement of each mass ratio.

We find that galaxies with the highest values of both M_{tot}/M_* and $M_{\text{tot}}/M_{\text{vis}}$ are in the blue cloud, are faint, and have low metallicities. Based on their luminosity and metallicity, these galaxies must be relatively early in their star formation histories. The addition of neutral hydrogen significantly reduces the value of $M_{\text{tot}}/M_{\text{vis}}$ relative to M_{tot}/M_* for these galaxies, implying that the feedback mechanism at the low-mass end of the stellar-halo mass relation is not as extreme as it appears.

We also observe an increase in both M_{tot}/M_* and $M_{\text{tot}}/M_{\text{vis}}$ for the brightest galaxies with high metallicities, typically members of the red sequence and green valley. The addition of neutral hydrogen has a smaller effect on $M_{\text{tot}}/M_{\text{vis}}$ relative to M_{tot}/M_* for this galaxy population compared to the faint, low metallicity galaxies. Due to their high metallicity, membership in the red sequence, and location in the BPT diagram, the star formation processes in these galaxies are likely to have been quenched by AGN activity. This AGN activity is also likely the cause for the increase in both M_{tot}/M_* and $M_{\text{tot}}/M_{\text{vis}}$ relative to intermediate-mass galaxies, having a similar impact as supernova feedback on low-mass galaxies.

We find that both M_{tot}/M_* and $M_{\text{tot}}/M_{\text{vis}}$ increase slightly with the distance to the nearest neighbor. This supports the idea that galaxy interactions have a tendency to increase the total visible mass of a galaxy.

Finally, we derive a parametrization with which we can predict M_{tot}/M_* based on easily accessible galaxy characteristics: the absolute magnitude and evolutionary classification. This empirical relationship can be applied in LSS studies to any galaxy with a known redshift and photometry.

ACKNOWLEDGEMENTS

The authors would like to thank Satya Gontcho A Gontcho for useful discussions and insightful questions, Eric Blackman for careful reading and thoughtful comments, and the anonymous referees for their detailed comments and suggestions. R.D. acknowledges support from the Department of Energy under the grant DE-SC0008475.0.

This project makes use of the MaNGA-Pipe3D data products. We thank the IA-UNAM MaNGA team for creating this catalogue, and the Conacyt Project CB-285080 for supporting them.

Funding for the Sloan Digital Sky Survey IV has been provided by the Alfred P. Sloan Foundation, the U.S. Department of Energy Office of Science, and the Participating Institutions. SDSS-IV acknowledges support and resources from the Center for High-Performance Com-

puting at the University of Utah. The SDSS web site is www.sdss.org.

SDSS-IV is managed by the Astrophysical Research Consortium for the Participating Institutions of the SDSS Collaboration including the Brazilian Participation Group, the Carnegie Institution for Science, Carnegie Mellon University, the Chilean Participation Group, the French Participation Group, Harvard-Smithsonian Center for Astrophysics, Instituto de Astrofísica de Canarias, The Johns Hopkins University, Kavli Institute for the Physics and Mathematics of the Universe (IPMU) / University of Tokyo, the Korean Participation Group, Lawrence Berkeley National Laboratory, Leibniz Institut für Astrophysik Potsdam (AIP), Max-Planck-Institut für Astronomie (MPIA Heidelberg), Max-Planck-Institut für Astrophysik (MPA Garching), Max-Planck-Institut für Extraterrestrische Physik (MPE), National Astronomical Observatories of China, New Mexico State University, New York University, University of Notre Dame, Observatório Nacional / MCTI, The Ohio State University, Pennsylvania State University, Shanghai Astronomical Observatory, United Kingdom Participation Group, Universidad Nacional Autónoma de México, University of Arizona, University of Colorado Boulder, University of Oxford, University of Portsmouth, University of Utah, University of Virginia, University of Washington, University of Wisconsin, Vanderbilt University, and Yale University.

REFERENCES

- Abazajian, K. N., Adelman-McCarthy, J. K., Agüeros, M. A., et al. 2009, *ApJS*, 182, 543, doi: [10.1088/0067-0049/182/2/543](https://doi.org/10.1088/0067-0049/182/2/543)
- Aguado, D. S., Ahumada, R., Almeida, A., et al. 2019, *The Astrophysical Journal Supplement Series*, 240, 23, doi: [10.3847/1538-4365/aaf651](https://doi.org/10.3847/1538-4365/aaf651)
- Aquino-Ortíz, E., Valenzuela, O., Sánchez, S. F., et al. 2018, *MNRAS*, 479, 2133, doi: [10.1093/mnras/sty1522](https://doi.org/10.1093/mnras/sty1522)
- Aquino-Ortíz, E., Sánchez, S. F., Valenzuela, O., et al. 2020, *ApJ*, 900, 109, doi: [10.3847/1538-4357/aba94e](https://doi.org/10.3847/1538-4357/aba94e)
- Avila-Reese, V., Zavala, J., Firmani, C., & Hernández-Toledo, H. M. 2008, *AJ*, 136, 1340, doi: [10.1088/0004-6256/136/3/1340](https://doi.org/10.1088/0004-6256/136/3/1340)
- Baldwin, J. A., Phillips, M. M., & Terlevich, R. 1981, *PASP*, 93, 5, doi: [10.1086/130766](https://doi.org/10.1086/130766)
- Barrera-Ballesteros, J. K., Heckman, T., Sánchez, S. F., et al. 2018, *ApJ*, 852, 74, doi: [10.3847/1538-4357/aa9b31](https://doi.org/10.3847/1538-4357/aa9b31)
- Bartelmann, M. 2010, *Classical and Quantum Gravity*, 27, 233001, doi: [10.1088/0264-9381/27/23/233001](https://doi.org/10.1088/0264-9381/27/23/233001)
- Behroozi, P., Wechsler, R. H., Hearin, A. P., & Conroy, C. 2019, *MNRAS*, 1134, doi: [10.1093/mnras/stz1182](https://doi.org/10.1093/mnras/stz1182)
- Blanton, M. R., Kazin, E., Muna, D., Weaver, B. A., & Price-Whelan, A. 2011, *AJ*, 142, 31, doi: [10.1088/0004-6256/142/1/31](https://doi.org/10.1088/0004-6256/142/1/31)
- Blanton, M. R., Lin, H., Lupton, R. H., et al. 2003, *AJ*, 125, 2276, doi: [10.1086/344761](https://doi.org/10.1086/344761)
- Blanton, M. R., Schlegel, D. J., Strauss, M. A., et al. 2005, *AJ*, 129, 2562, doi: [10.1086/429803](https://doi.org/10.1086/429803)
- Bosma, A. 1978, PhD thesis, Groningen University
- Brown, J. S., Martini, P., & Andrews, B. H. 2016, *MNRAS*, 458, 1529, doi: [10.1093/mnras/stw392](https://doi.org/10.1093/mnras/stw392)
- Bundy, K., Bershadsky, M. A., Law, D. R., et al. 2015, *ApJ*, 798, 7, doi: [10.1088/0004-637X/798/1/7](https://doi.org/10.1088/0004-637X/798/1/7)
- Cappellari, M., Bacon, R., Bureau, M., et al. 2006, *MNRAS*, 366, 1126, doi: [10.1111/j.1365-2966.2005.09981.x](https://doi.org/10.1111/j.1365-2966.2005.09981.x)
- Carignan, C., & Freeman, K. C. 1985, *ApJ*, 294, 494, doi: [10.1086/163316](https://doi.org/10.1086/163316)

- Cherinka, B., Andrews, B. H., Sánchez-Gallego, J., et al. 2019, *AJ*, 158, 74, doi: [10.3847/1538-3881/ab2634](https://doi.org/10.3847/1538-3881/ab2634)
- Choi, Y.-Y., Han, D.-H., & Kim, S. S. 2010, *Journal of Korean Astronomical Society*, 43, 191, doi: [10.5303/JKAS.2010.43.6.191](https://doi.org/10.5303/JKAS.2010.43.6.191)
- Coenda, V., Martínez, H. J., & Muriel, H. 2018, *MNRAS*, 473, 5617, doi: [10.1093/mnras/stx2707](https://doi.org/10.1093/mnras/stx2707)
- Di Paolo, C., Salucci, P., & Erkurt, A. 2019, *MNRAS*, 490, 5451, doi: [10.1093/mnras/stz2700](https://doi.org/10.1093/mnras/stz2700)
- Domínguez Sánchez, H., Huertas-Company, M., Bernardi, M., Tuccillo, D., & Fischer, J. L. 2018, *MNRAS*, 476, 3661, doi: [10.1093/mnras/sty338](https://doi.org/10.1093/mnras/sty338)
- Douglass, K. A. 2017, PhD thesis, Drexel University
- Douglass, K. A., Smith, J. A., & Demina, R. 2019, *ApJ*, 886, 153, doi: [10.3847/1538-4357/ab4bce](https://doi.org/10.3847/1538-4357/ab4bce)
- Drory, N., MacDonald, N., Bershadsky, M. A., et al. 2015, *AJ*, 149, 77, doi: [10.1088/0004-6256/149/2/77](https://doi.org/10.1088/0004-6256/149/2/77)
- Ferrero, I., Navarro, J. F., Abadi, M. G., et al. 2017, *MNRAS*, 464, 4736, doi: [10.1093/mnras/stw2691](https://doi.org/10.1093/mnras/stw2691)
- Freeman, K. C. 1970, *ApJ*, 160, 811, doi: [10.1086/150474](https://doi.org/10.1086/150474)
- Fukugita, M., Ichikawa, T., Gunn, J. E., et al. 1996, *AJ*, 111, 1748, doi: [10.1086/117915](https://doi.org/10.1086/117915)
- Gunn, J. E., Carr, M., Rockosi, C., et al. 1998, *AJ*, 116, 3040, doi: [10.1086/300645](https://doi.org/10.1086/300645)
- Haynes, M. P., Giovanelli, R., Kent, B. R., et al. 2018, *ApJ*, 861, 49, doi: [10.3847/1538-4357/aac956](https://doi.org/10.3847/1538-4357/aac956)
- Jian, H.-Y., Lin, L., Koyama, Y., et al. 2020, *ApJ*, 894, 125, doi: [10.3847/1538-4357/ab86a8](https://doi.org/10.3847/1538-4357/ab86a8)
- Karukes, E. V., & Salucci, P. 2017, *MNRAS*, 465, 4703, doi: [10.1093/mnras/stw3055](https://doi.org/10.1093/mnras/stw3055)
- Kauffmann, G., Heckman, T. M., Tremonti, C., et al. 2003, *MNRAS*, 346, 1055, doi: [10.1111/j.1365-2966.2003.07154.x](https://doi.org/10.1111/j.1365-2966.2003.07154.x)
- Kewley, L. J., Dopita, M. A., Sutherland, R. S., Heisler, C. A., & Trevena, J. 2001, *ApJ*, 556, 121, doi: [10.1086/321545](https://doi.org/10.1086/321545)
- Lupton, R., Gunn, J. E., Ivezić, Z., Knapp, G. R., & Kent, S. 2001, in *Astronomical Society of the Pacific Conference Series*, Vol. 238, *Astronomical Data Analysis Software and Systems X*, ed. J. Harnden, F. R., F. A. Primini, & H. E. Payne, 269
- Martin, D. C., Wyder, T. K., Schiminovich, D., et al. 2007, *ApJS*, 173, 342, doi: [10.1086/516639](https://doi.org/10.1086/516639)
- Martizzi, D., Vogelsberger, M., Torrey, P., et al. 2020, *MNRAS*, 491, 5747, doi: [10.1093/mnras/stz3418](https://doi.org/10.1093/mnras/stz3418)
- Moster, B. P., Somerville, R. S., Maubetsch, C., et al. 2010, *ApJ*, 710, 903, doi: [10.1088/0004-637X/710/2/903](https://doi.org/10.1088/0004-637X/710/2/903)
- Oman, K. A., Marasco, A., Navarro, J. F., et al. 2019, *MNRAS*, 482, 821, doi: [10.1093/mnras/sty2687](https://doi.org/10.1093/mnras/sty2687)
- Ouellette, N. N. Q., Courteau, S., Holtzman, J. A., et al. 2017, *ApJ*, 843, 74, doi: [10.3847/1538-4357/aa74b1](https://doi.org/10.3847/1538-4357/aa74b1)
- Park, C., & Choi, Y.-Y. 2005, *ApJL*, 635, L29, doi: [10.1086/499243](https://doi.org/10.1086/499243)
- Persic, M., Salucci, P., & Stel, F. 1996, *MNRAS*, 281, 27, doi: [10.1093/mnras/281.1.27](https://doi.org/10.1093/mnras/281.1.27)
- Planck Collaboration, Aghanim, N., Akrami, Y., et al. 2020, *A&A*, 641, A6, doi: [10.1051/0004-6361/201833910](https://doi.org/10.1051/0004-6361/201833910)
- Randriamampandry, T. H., Combes, F., Carignan, C., & Deg, N. 2015, *MNRAS*, 454, 3743, doi: [10.1093/mnras/stv2147](https://doi.org/10.1093/mnras/stv2147)
- Salim, S. 2014, *Serbian Astronomical Journal*, 189, 1, doi: [10.2298/SAJ1489001S](https://doi.org/10.2298/SAJ1489001S)
- Salucci, P. 2019, *A&A Rv*, 27, 2, doi: [10.1007/s00159-018-0113-1](https://doi.org/10.1007/s00159-018-0113-1)
- Sánchez, S. F., Pérez, E., Sánchez-Blázquez, P., et al. 2016, *RMxAA*, 52, 171
- Sánchez, S. F., Avila-Reese, V., Hernandez-Toledo, H., et al. 2018, *RMxAA*, 54, 217
- Sofue, Y. 2013, *Mass Distribution and Rotation Curve in the Galaxy*, ed. T. D. Oswalt & G. Gilmore, Vol. 5, 985
- Springel, V., White, S. D. M., Jenkins, A., et al. 2005, *Nature*, 435, 629, doi: [10.1038/nature03597](https://doi.org/10.1038/nature03597)
- Stark, D. V., Masters, K. L., Avila-Reese, V., et al. 2021, *MNRAS*, 503, 1345, doi: [10.1093/mnras/stab566](https://doi.org/10.1093/mnras/stab566)
- Strauss, M. A., Weinberg, D. H., Lupton, R. H., et al. 2002, *AJ*, 124, 1810, doi: [10.1086/342343](https://doi.org/10.1086/342343)
- Strigari, L. E., Bullock, J. S., Kaplinghat, M., et al. 2008, *Nature*, 454, 1096, doi: [10.1038/nature07222](https://doi.org/10.1038/nature07222)
- Torres-Flores, S., Epinat, B., Amram, P., Plana, H., & Mendes de Oliveira, C. 2011, *MNRAS*, 416, 1936, doi: [10.1111/j.1365-2966.2011.19169.x](https://doi.org/10.1111/j.1365-2966.2011.19169.x)
- Tremonti, C. A., Heckman, T. M., Kauffmann, G., et al. 2004, *ApJ*, 613, 898, doi: [10.1086/423264](https://doi.org/10.1086/423264)
- Tully, R. B., & Fisher, J. R. 1977, *A&A*, 54, 661
- Valenzuela, O., Rhee, G., Klypin, A., et al. 2007, *ApJ*, 657, 773, doi: [10.1086/508674](https://doi.org/10.1086/508674)
- Wake, D. A., Bundy, K., Diamond-Stanic, A. M., et al. 2017, *AJ*, 154, 86, doi: [10.3847/1538-3881/aa7ecc](https://doi.org/10.3847/1538-3881/aa7ecc)
- Wechsler, R. H., & Tinker, J. L. 2018, *ARA&A*, 56, 435, doi: [10.1146/annurev-astro-081817-051756](https://doi.org/10.1146/annurev-astro-081817-051756)
- Weiner, B. J., Willmer, C. N. A., Faber, S. M., et al. 2006, *ApJ*, 653, 1027, doi: [10.1086/508921](https://doi.org/10.1086/508921)